Article

Study on the Luminescence Performance and Anti-Counterfeiting Application of Eu^{2+}, Nd^{3+} Co-Doped $SrAl_2O_4$ Phosphor

Zhanpeng Wang [1], Quanxiao Liu [1,*], Jigang Wang [1,*], Yuansheng Qi [1], Zhenjun Li [2,3,*], Junming Li [4], Zhanwei Zhang [5], Xinfeng Wang [5], Cuijuan Li [5] and Rong Wang [5]

[1] Beijing Key Laboratory of Printing and Packaging Materials and Technology, Beijing Institute of Graphic Communication, Beijing 102600, China; wzpbigc@163.com (Z.W.); yuansheng-qi@bigc.edu.cn (Y.Q.)
[2] National Center for Nanoscience and Technology, CAS Key Laboratory of Nanophotonic Materials and Devices (Preparatory), Beijing 100190, China
[3] The GBA Research Innovation Institute for Nanotechnology, Guangzhou 510700, China
[4] Beijing Key Laboratory for Sensors, Beijing Information Science & Technology University, Beijing 100192, China; li@bistu.edu.cn
[5] Yunnan Jiake Packaging Technology Co., Ltd., Yuxi 653100, China; zhang13930678816@163.com (Z.Z.); wangxinfeng88331@gmail.com (X.W.); licuijuan1982@163.com (C.L.); wangrong6355@126.com (R.W.)
* Correspondence: liuquanxiao@bigc.edu.cn (Q.L.); jigangwang@bigc.edu.cn (J.W.); lizhenjun@nanoctr.cn (Z.L.)

Abstract: This manuscript describes the synthesis of green long afterglow nanophosphors $SrAl_2O_4$:Eu^{2+}, Nd^{3+} using the combustion process. The study encompassed the photoluminescence behavior, elemental composition, chemical valence, morphology, and phase purity of $SrAl_2O_4$:Eu^{2+}, Nd^{3+} nanoparticles. The results demonstrate that after introducing Eu^{2+} into the matrix lattice, it exhibits an emission band centered at 508 nm when excited by 365 nm ultraviolet light, which is induced by the $4f^65d^1 \rightarrow 4f^7$ transition of Eu^{2+} ions. The optimal doping concentrations of Eu^{2+} and Nd^{3+} were determined to be 2% and 1%, respectively. Based on X-ray diffraction (XRD) analysis, we have found that the physical phase was not altered by the doping of Eu^{2+} and Nd^{3+}. Then, we analyzed and compared the quantum yield, fluorescence lifetime, and afterglow decay time of the samples; the co-doped ion Nd^{3+} itself does not emit light, but it can serve as an electron trap center to collect a portion of the electrons produced by the excitation of Eu^{2+}, which gradually returns to the ground state after the excitation stops, generating an afterglow luminescence of about 15 s. The quantum yields of $SrAl_2O_4$:Eu^{2+} and $SrAl_2O_4$:Eu^{2+}, Nd^{3+} phosphors were 41.59% and 10.10% and the fluorescence lifetimes were 404 ns and 76 ns, respectively. In addition, the E_g value of 4.98 eV was determined based on the diffuse reflectance spectra of the material, which closely matches the calculated bandgap value of $SrAl_2O_4$. The material can be combined with polyacrylic acid to create optical anti-counterfeiting ink, and the butterfly and ladybug patterns were effectively printed through screen printing; this demonstrates the potential use of phosphor in the realm of anti-counterfeiting printing.

Keywords: long afterglow; $SrAl_2O_4$:Eu^{2+}, Nd^{3+}; combustion method; screen printing; anti-counterfeiting

1. Introduction

Doping of nanomaterials with rare earth ions can change their morphology, crystalline phase, size, and electronic configuration, endowing nanomaterials with excellent optical, electrical, and magnetic characteristics. Rare-earth-doped long afterglow luminescent materials quickly absorb energy and promptly generate light when stimulated by an excitation light source. They continue to emit light for a significant duration even after the removal of the excitation light source [1]. Due to its high initial brightness, long fluorescence lifetime, energy saving, and environmental protection, it has been widely

used in bio-imaging [2], catalysis [3], environmental remediation [4], anti-counterfeiting [5], and optical information storage [6]. Among many phosphorescent materials, the crystal structure and material composition of $SrAl_2O_4$ have been extensively investigated, owing to its distinctive properties such as excellent fluorescence performance and long-lasting afterglow [7]. During the early 20th century, ZnS:Cu was used as a long afterglow phosphor, but there were problems such as insufficient brightness, short afterglow time, and not being environmentally friendly. The study of $SrAl_2O_4$ began in 1996 when Japanese scientists first developed green long afterglow phosphors co-doped with Eu^{2+} and Dy^{3+} in $SrAl_2O_4$ [8]. In $SrAl_2O_4$:Eu^{2+}, Dy^{3+}, the Eu^{2+} serves as a luminescent center and Dy^{3+} serves as a trap center to capture electrons and produce a longer afterglow [9]. Since then, in recent decades, researchers have attempted to prepare a series of rare earth luminescent materials based on $SrAl_2O_4$ by different synthesis methods or doped with different rare earth ions [10]. For example, the sol-gel method was employed to prepare $SrAl_2O_4$:Tb^{3+} green long afterglow phosphor [11]; $SrAl_2O_4$:Ce^{3+} phosphors for white light LEDs were prepared by the high-temperature solid-phase method [12]; $SrAl_2O_4$:Eu^{2+}, Dy^{3+} luminescent materials have been synthesized using hydrothermal and surfactant–template methods [13]; $SrAl_2O_4$:Eu^{3+} red phosphor was prepared by the combustion method [14]. In numerous studies, Eu^{2+} is commonly used as the luminescent center of $SrAl_2O_4$ phosphor, and Re^{3+} co-doping improves its luminescence and long afterglow performance [15–18]. $SrAl_2O_4$:Eu^{2+}, Nd^{3+} is one of them, and it has received widespread attention in recent years. Ryu et al. synthesized $SrAl_2O_4$:Eu^{2+}, Nd^{3+} luminescent materials by the traditional high-temperature solid-phase method [19], and Marchal et al. prepared $SrAl_2O_4$:Eu^{2+}, Nd^{3+} long afterglow luminescent materials for ceramic pigments by the sol-gel method [20], but there are problems such as long reaction time. The preparation of $SrAl_2O_4$:Eu^{2+}, Nd^{3+} materials by the single-step solution combustion method can significantly reduce the reaction time and cost.

Counterfeit and shoddy goods are emerging, causing serious economic losses to consumers and enterprises. The counterfeited medicines, food, etc., may even threaten consumers' health and life safety [21]. In this context, anti-counterfeiting technology breaks through the field of banknotes, checks, bonds, stocks, and other securities, and its application in the field of commodity packaging is becoming more and more extensive, for example, hologram anti-counterfeiting, QR code tracking and traceability, optical anti-counterfeiting, watermark design, preparation of anti-counterfeiting ink [22–26], and so on. Among them, the anti-counterfeiting inks prepared by rare earth long afterglow phosphors are applied in the field of printing anti-counterfeiting labels and other fields because of their bright colors, adjustable brightness, and long fluorescence life [27–30]. The anti-counterfeiting inks are transparent in color under fluorescent light, absorb energy, start to glow after being stimulated, and still can keep the glow for a period of time after withdrawing the stimulation source, which greatly increases the security and feasibility of anti-counterfeit packaging.

In this study, $SrAl_2O_4$:Eu^{2+}, Nd^{3+} long afterglow phosphors with optimal doping concentration and reaction temperature were prepared by the combustion method, and we conducted a comprehensive analysis of their photoluminescence, bandgap, crystal structures, elemental compositions, elemental valence, fluorescence lifetimes, and quantum yields. The compound $SrAl_2O_4$:Eu^{2+}, Nd^{3+} was subsequently synthesized for the purpose of creating ink that can be used for anti-counterfeiting measures. This ink was then applied to the packaging using screen printing techniques, showcasing the material's capability for anti-counterfeiting applications.

2. Experimental Methods

2.1. Materials and Preparation

The combustion method was employed to prepare a series of $Sr_{1-x-y}Al_2O_4$:xEu^{2+}, yNd^{3+} (x = 0, 0.01, 0.02, 0.03, 0.05, 0.08; y = 0.005, 0.01, 0.02, 0.03, 0.05, 0.08) phosphors. Eu_2O_3 (purity: 99.99%), Al_2O_3 (purity: 99.99%), Sr_2CO_3 (purity: 99.99%), Nd_2O_3 (purity: 99.99%), HNO_3 (purity: 80%), and urea (purity: 99.99%) were utilized as the raw material,

all of which were acquired from Tianjin Chemical Reagent Factory. The chemicals can be directly used for experiments without any additional drying or purifying steps.

2.2. Synthesis of Materials

Initially, precise quantities of nitric acid (HNO_3) and purified water were introduced to Eu_2O_3, Al_2O_3, Sr_2CO_3, and Nd_2O_3 to prepare $Sr(NO_3)_2$ (0.5 mmol/mL), $Al(NO_3)_3$ (1 mmol/mL), $Eu(NO_3)_3$ (0.1 mmol/mL), and $Nd(NO_3)_3$ (0.5 mmol/mL) solutions, respectively. Subsequently, we used a pipette to measure a specific quantity of reagent into a crucible in accordance with the stoichiometric ratio. Then, 2.2 g of urea particles was added as a reducing and combustion agent and thoroughly mixed until the urea had completely dissolved. Following that, the mixture was placed in a muffle furnace that had been preheated, and it was permitted to burn completely. After approximately 5 min, we extracted the substance and obtained a white solid that was loose and distended. Ultimately, the temperature of the sample was lowered to the ambient temperature of the room, and the substance was ground for a duration of 15–30 min until it became a fine powder, and it was transferred into a test tube for later testing.

The concentrations of Eu^{2+} in the $SrAl_2O_4$:Eu^{2+} material that was synthesized are 0%, 1%, 2%, 3%, 5%, and 8%, respectively. The concentrations of Nd^{3+} in $SrAl_2O_4$:0.02Eu^{2+} and Nd^{3+} materials are 0.5%, 1%, 2%, 3%, 5%, and 8%, respectively. Following the determination of the optimal ion doping concentration, the same experimental method was employed to prepare the samples at reaction temperatures of 500 °C, 600 °C, 700 °C, 800 °C, and 900 °C in order to identify the optimal reaction temperature.

2.3. Anti-Counterfeit Ink Preparation

The $SrAl_2O_4$:Eu^{2+}, Nd^{3+} phosphor, after preparation, was introduced into a mixture containing ethanol and polyacrylic acid. The amount of phosphor added was adjusted to attain a viscosity appropriate for screen printing. A glass rod was employed to stir the mixture continuously, ensuring the even dispersion of the phosphor in the solution, resulting in the creation of the anti-counterfeit ink. Figure 1 shows a schematic diagram illustrating the process of producing phosphor and anti-counterfeit ink, as well as screen printing.

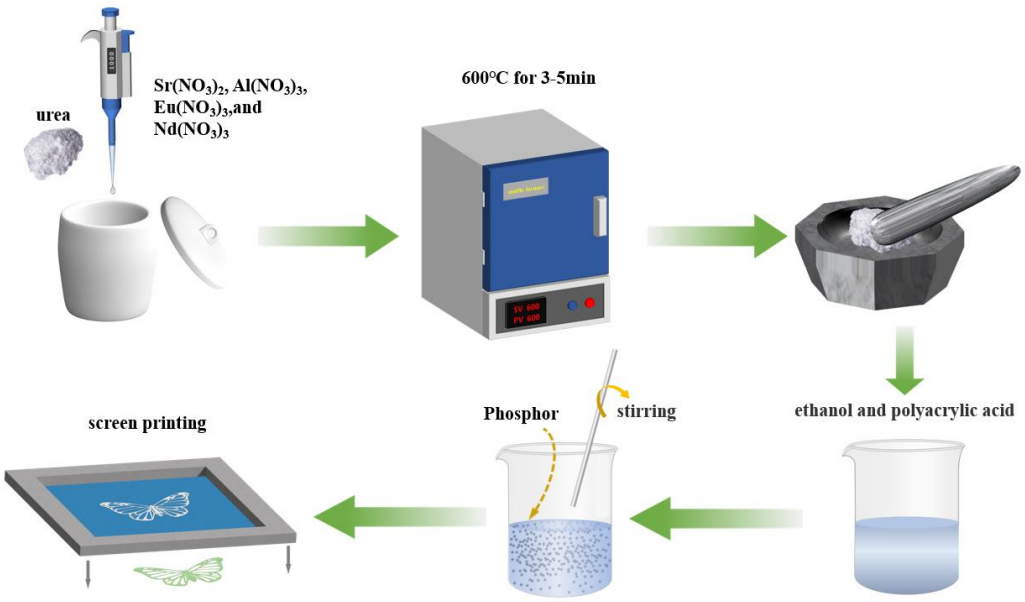

Figure 1. Flow process diagram of phosphor preparation and screen printing.

2.4. Characterizing Instruments

The powder X-ray diffractometer (D/max 2200PC by Rigaku, The Woodlands, TX, USA) was used to record the crystal structures of the synthesized samples, which ranged

from 10° to 70°, with Cu Kα radiation (λ = 1.54 Å). The binding energy was determined using X-ray photoelectron spectroscopy (XPS, Monochromatic AI Kα(hv = 1486.6 eV) ESCALAB 250 XI, 150W, 650 μm, Waltham, MA, USA). The phosphor morphology was examined using scanning electron microscopy (Quanta 250 FEG, Hitachi, Tokyo, Japan). The elemental compositions and contents were determined using a scanning electron microscope (Thermo Fisher Scientific, Waltham, MA, USA). A fluorescence spectrometer (F4700, Hitachi, Japan) was utilized to conduct photoluminescence spectroscopy (PL) and photoluminescence excitation spectroscopy (PLE). The UV diffuse reflectance absorption spectra were obtained using a UV-3600 Ultraviolet-Visible Near-Infrared Spectrophotometer (Shimadzu Corporation, Kyoto, Japan). The quantum yield, fluorescence lifetime, and afterglow decay curves of phosphors were quantified using a transient steady-state fluorescence spectrometer (Hamamatsu Photonics Quantaurus-Tau C16361-2, Chiyoda, Japan).

3. Results and Discussion

3.1. XRD Structure Analysis

X-ray diffraction was employed to investigate the physical phase composition and purity of $SrAl_2O_4$ phosphors at varying ion doping concentrations and reaction temperatures. Figure 2a shows the x-ray diffraction (XRD) structure of the $SrAl_2O_4$:0.02Eu^{2+}, xNd^{3+} nanophosphors (x = 0.005, 0.01, 0.02, 0.03, 0.05, 0.08) synthesized by calcination at 600 °C and standard cards of the $SrAl_2O_4$ (PDF#97-016-0296). We can observe that the XRD profile exhibits distinct peaks, and that these peaks closely correspond to the data recorded in the standard cards of the $SrAl_2O_4$ (PDF#97-016-0296). The lattice constant of the synthesized sample was measured as a = 8.450Å, b = 8.752Å, c = 5.109Å, β = 93.4° using the JADE 9.0 software. The presence of these peaks can be ascribed to the X-ray reflections originating from the monoclinic $SrAl_2O_4$ crystallographic planes (011), (121), (−211), (221), (210), and (031). Figure 2b shows the XRD patterns of $SrAl_2O_4$:0.02Eu^{2+}, 0.01Nd^{3+} nanophosphors obtained by calcination at different temperatures. The diffraction peaks' positions are essentially unchanged in comparison to Figure 2a, suggesting that the crystal phase of the $SrAl_2O_4$ host is not affected by the co-doping of Eu^{2+} and Nd^{3+} ions.

We also performed Rietveld refinement analysis of XRD data of $SrAl_2O_4$:0.02Eu^{2+}, 0.01Nd^{3+} phosphors obtained by calcination at 600 °C using the General Structure Analysis System-II (GSAS-2) software. As shown in Figure 2c, it can be found that the observed data points and the calculated data curves are in good agreement, and no additional impurity peaks are generated. For the $SrAl_2O_4$:0.02Eu^{2+}, 0.01Nd^{3+} phosphors, R_{wp} = 7.04%, and R_p = 4.91% represent the physical and mathematical fit between the sample results and the standard card data, both of which are less than 10%, indicating a favorable curve fitting. From this, we can conclude that the prepared samples are still in single-phase structure with high purity and have no impurities. In addition, Eu^{2+} and Nd^{3+} in the material have a propensity to substitute the Sr^{2+} sites in the main lattice of $SrAl_2O_4$ [31–34].

In addition, based on the data provided by the XRD pattern, we used Origin 2022 software to fit the XRD pattern using the Gaussian formula, obtained the peak position radians and widths, and calculated the grain size of the sample using the famous Scherrer formula [35]:

$$D = \frac{k\lambda}{\beta cos\theta} \quad (1)$$

where k is Scherrer constant with a value of 0.89, λ is the wavelength of the radiation with a value of 0.1546, β and θ represent the FWHM (radians) and the position of the peak, respectively, which have been fitted and calculated by Origin software, and D is the grain size. The average grain sizes of the samples prepared at different temperatures (500–900 °C) were calculated to be 30.593, 33.846, 30.702, 31.227, and 31.338 nm, respectively. In addition, we also calculated the lattice spacing, micro-strain, and dislocation density of the samples, as shown in Table 1.

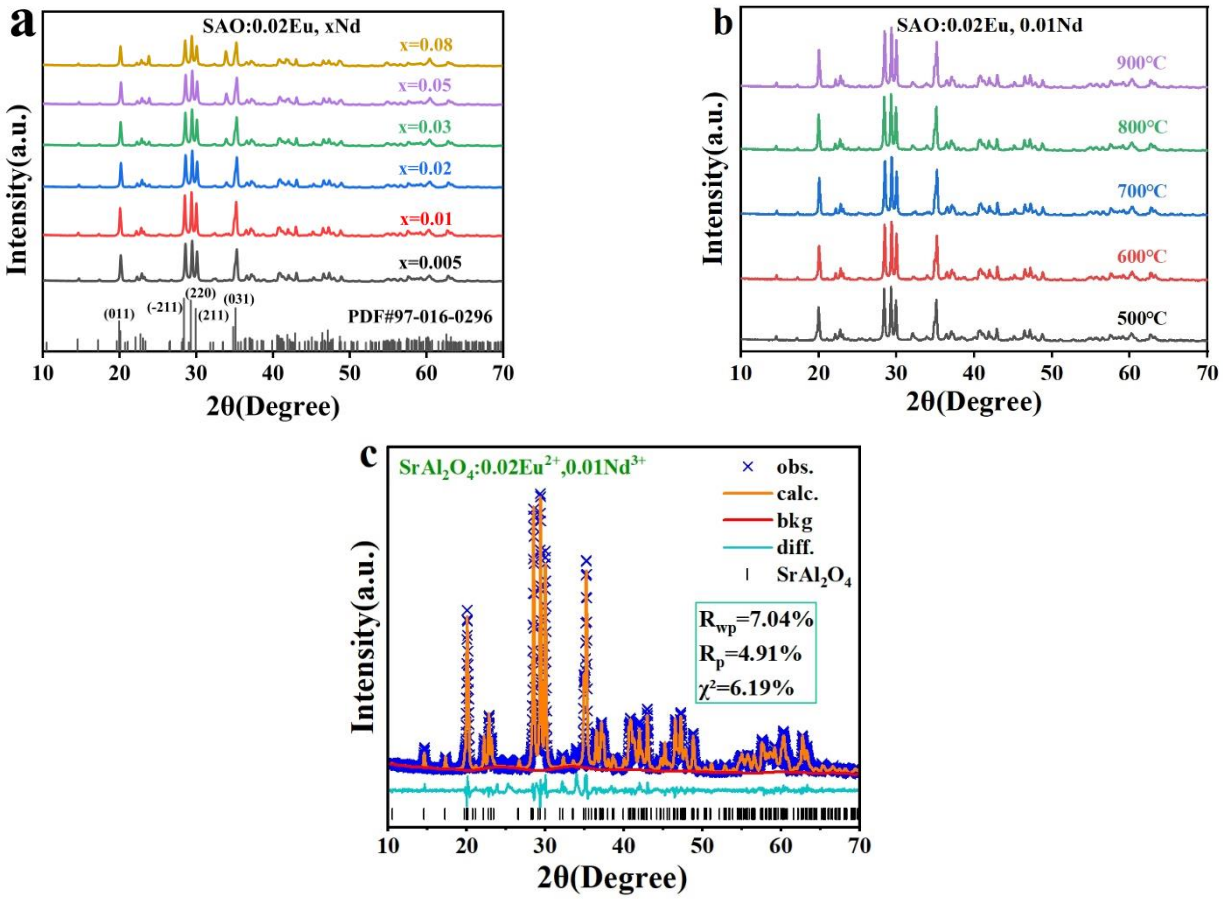

Figure 2. (**a**) The XRD structures of $SrAl_2O_4$:0.02Eu^{2+}, xNd^{3+} (x = 0.005, 0.01, 0.02, 0.03, 0.05, 0.08) phosphors. (**b**) The XRD structures of $SrAl_2O_4$:0.02Eu^{2+}, 0.01Nd^{3+} at different sintering temperatures (500, 600, 700, 800, 900 °C). (**c**) Rietveld refinement of the $SrAl_2O_4$:0.02Eu^{2+}, 0.01Nd^{3+} phosphor.

Table 1. XRD data of $SrAl_2O_4$:Eu^{2+}, Nd^{3+} phosphor.

2θ	FWHM (β)	Lattic Spacing (d)	Intensity (I)	hkl	Crystallite Size (D)	Dislocation Density (δ)	Micro-Strain (ε)
20.066	0.257	0.442	60	011	31.010	1.040	6.345
28.487	0.222	0.313	95	−211	36.589	0.747	3.808
29.370	0.206	0.304	100	220	39.424	0.643	3.430
30.002	0.204	0.298	79	211	39.775	0.632	3.330
35.147	0.367	0.255	67	031	22.430	1.988	5.062

3.2. Elemental Analysis

Since the luminescence efficacy of the materials is directly influenced by the valence states of the doped elements Eu and Nd, we measured the binding energies of the elements in the prepared $SrAl_2O_4$:0.02Eu^{2+}, 0.01Nd^{3+} luminescent materials by using X-ray photoelectron spectroscopy (XPS), and conducted comparative analyses to determine the valence states of the doped elements. The XPS measurements, as illustrated in Figure 3a, demonstrate binding energies that correspond to Sr 3d, Al 2p, O 1s, C 1s, Eu 3d, and Nd 3d. Figure 3b displays the high-resolution (HR) XPS spectra of Sr 3d. The peak binding energies of Sr 3d are observed to be 133.60 eV and 135.24 eV, which is consistent with that of Sr $3d_{5/2}$ and Sr $3d_{3/2}$ [36,37], respectively. This is related to the occupancy of Sr elements in $SrAl_2O_4$ [38]. Figure 3e illustrates the binding energy of Eu 3d peaks at 1125.95 eV for Eu^{2+} $3d_{5/2}$ and at 1155.06 eV for Eu^{2+} $3d_{3/2}$, which demonstrates that the Eu ions in the prepared $SrAl_2O_4$:0.02Eu^{2+}, 0.01Nd^{3+} luminescent materials are in the divalent oxidation

state [39,40]. Figure 3f shows that the peak binding energies of Nd 3d are 977.83 eV and 1000.31 eV, which is consistent with that of Nd^{3+} $3d_{5/2}$ and Nd^{3+} $3d_{3/2}$ [41–43]. In addition, we employed Avantage 5.9 software to analyze and calculate the XPS data of the substance, resulting in the determination of the atomic ratios of $SrAl_2O_4$:Eu^{2+}, Nd^{3+} powders. The measured data are incongruous with the EDS test results, attributable to the disparate testing principles employed by the two methods, as shown in Table 2. This also proves the difference in element distribution between the surface and volume of the sample, which is caused by the combustion method. This reaction may result in an uneven distribution of elements within the material.

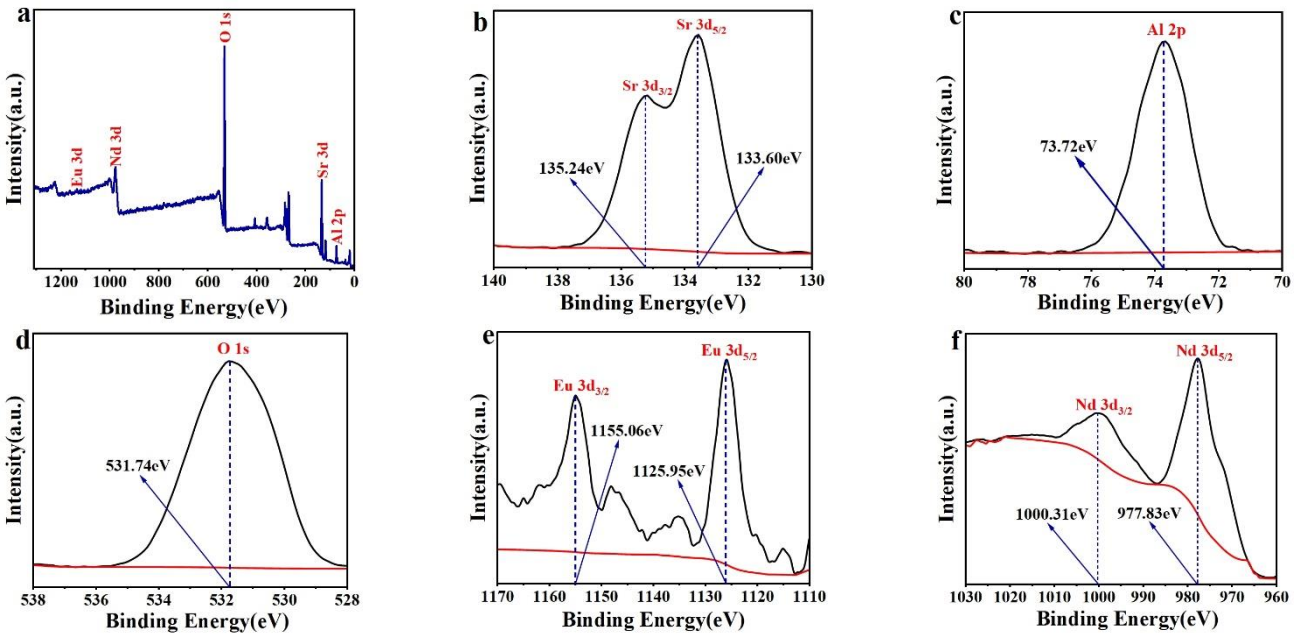

Figure 3. (**a**) The XPS spectra of $SrAl_2O_4$:Eu^{2+}, Nd^{3+}; (**b**–**f**) the high-resolution (HR) XPS spectra of Sr 3d, Al 2p, O 1s, Eu 3d, and Nd 3d.

Table 2. The atomic ratio of $SrAl_2O_4$:Eu^{2+}, Nd^{3+} phosphor.

Method	Atomic%				
	Sr	Al	O	Eu	Nd
XPS	9.90	20.16	66.50	0.77	2.67
EDS	10.40	31.20	57.90	0.30	0.20

3.3. SEM Analysis

Scanning electron microscopy (SEM) was employed to examine the impact of temperature on the surface morphology of the samples. Figure 4a–e depict the SEM images of $SrAl_2O_4$:$0.02Eu^{2+}$, $0.01Nd^{3+}$ luminescent materials produced at different reaction temperatures; the magnification is 10,000×, with an average scale size of approximately 1 μm. From the figure, it can be observed that there are many cracks and pores on the surface of the sample, which are caused by the violent reaction that occurs in a short period of time during the combustion method [17,44]. During the combustion process, many gases are released, leading to this phenomenon. Similarly, we observed the aggregation of sample particles into clustered structures, which reflects the intrinsic behavior of combustion. The particles in the powder are uneven and their sizes are not exactly the same; this could be attributed to the inhomogeneous temperature distribution of the sample during the reaction [45], uneven mass flow distribution, and differences in the degree of grinding [46]. We can also observe that the sample prepared at 500 °C has larger pore gaps. When the reaction temperature reaches 600 °C, the pores between the sample particles gradually become smaller, and the

particle size is relatively regular and uniform. As the temperature further increases, the pores between the sample particles become larger and the size becomes more uneven. The structural variations can affect the absorption and emission process of light, which explains why the sample prepared at 600 °C has the highest luminescence intensity. Moreover, different reaction temperatures can also affect the distribution of dopants, thereby affecting luminescence [47–49].

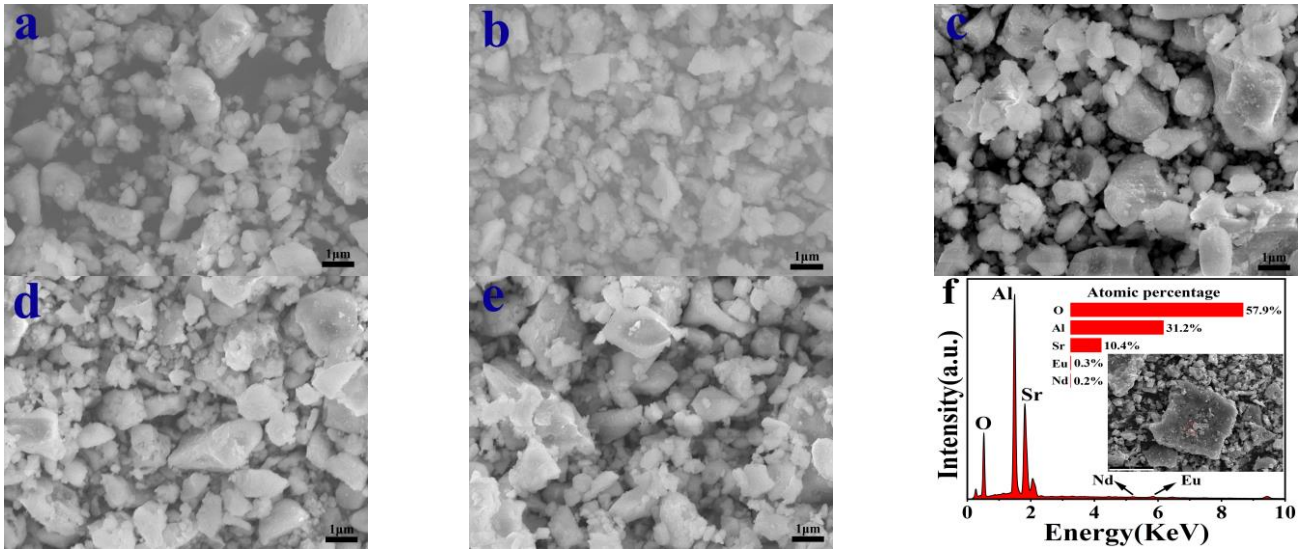

Figure 4. SEM images of $SrAl_2O_4$:0.02Eu^{2+}, 0.01Nd^{3+} synthesized at (**a**) 500 °C, (**b**) 600 °C, (**c**) 700 °C, (**d**) 800 °C, (**e**) 900 °C. (**f**) The EDS of $SrAl_2O_4$:0.02Eu^{2+}, 0.01Nd^{3+} powder prepared at 600 °C.

Furthermore, the presence of the elements Sr, Al, O, Eu, and Nd is confirmed by the Energy Dispersive X-ray Spectroscopy (EDS) spectra of $SrAl_2O_4$:0.02Eu^{2+}, 0.01Nd^{3+}, as depicted in Figure 4f. The elemental composition of the material and the energy spectrum intensity signals of each element were determined by measuring small areas of the sample. The chemical composition of $SrAl_2O_4$:0.02Eu^{2+}, 0.01Nd^{3+} is essentially consistent with the spectral intensity signals of Sr, Al, O, Eu, and Nd. The proportion of Eu and Nd elements in the sample is slightly higher than the standard value of the sample chemical formula, possibly as a result of the combustion method used in this study. This method completes the doping process in a shorter amount of time through solution combustion, which results in a more violent reaction. This reaction may result in an uneven distribution of elements within the material. The EDS detected the presence of Eu and Nd, indicating that Eu and Nd were successfully doped into the host material.

3.4. Photoluminescence Analysis

Figure 5 displays the spectra of photoluminescence (PL) and photoluminescence excitation (PLE) for $SrAl_2O_4$ luminescent materials. These materials were produced using various ion doping concentrations and reaction temperatures. Figure 5 depicts the fluorescence emission spectra of $Sr_{1-x}Al_2O_4$:xEu^{2+} (x = 0, 0.01, 0.02, 0.03, 0.05, 0.08) at 365 nm excitation wavelength, and the combustion temperature is 600 °C. It is evident that the luminescence intensity of the samples increased progressively as the concentration of Eu^{2+} increased, and peaked at 3% Eu^{2+} concentration, after which the luminescence intensity gradually decreased. The spectrum exhibits a wide emission band in the green region, with a peak at 508 nm. An increase in the concentration of Eu^{2+} does not change the peak location of the emission spectrum of the luminescent material, but it does impact the luminescence intensity of the sample, which is attributable to the transition of the Eu^{2+} ion from the high-energy state $4f^65d$ to the low-energy state $4f^7$. Similarly, Figure 5b displays the fluorescence emission spectra of $Sr_{0.98-y}Al_2O_4$:0.02Eu^{2+}, yNd^{3+} (y = 0.005, 0.01, 0.02, 0.03, 0.05, 0.08) at 365 nm excitation wavelength with a reaction temperature of 600 °C.

When the doping concentration of Nd^{3+} is 1%, the luminescence intensity of the sample is at its highest, and the maximal emission peak is also at 508 nm, as illustrated in the figure. After determining the optimal ion doping concentration, we prepared $SrAl_2O_4$:0.02Eu^{2+}, 0.01Nd^{3+} luminescent materials with different temperatures, and their photoluminescence spectra are shown in Figure 5c. The luminescence intensity of the material is significantly influenced by the reaction temperature; the luminescence intensity of the sample is at its highest when the reaction temperature is 600 °C, as illustrated in the figure. The photoluminescence excitation (PLE) spectra of the samples after excitation are depicted in Figure 5d. The PLE spectra exhibit a paragraph absorption band that is centered at 365 nm, consistent with the emission spectra, and corresponds to the $4f^7 \rightarrow 4f^6 5d$ transition of the Eu^{2+}.

The monoclinic crystal structure of $SrAl_2O_4$ contains two distinct Sr sites, Sr1 and Sr2, which are essentially identical in size [50]. During the doping process, given the comparable ionic radii of Eu^{2+} and Sr^{2+}, Eu^{2+} tends to substitute for Sr^{2+} in $SrAl_2O_4$. Eu^{2+} at both sites undergoes a 4f→5d transition, resulting in luminescence [51]. In addition, the samples doped with Eu^{2+} and Nd^{3+} did not exhibit any emission properties from the Nd^{3+} ions. This indicates that Nd^{3+} may not function as a source of luminescence, but instead may serve as a center for trapping. Nd^{3+} releases stored energy for sustained luminescence after cessation of excitation [52]. An increase in the concentration of Nd^{3+} ions leads to the generation of a greater number of electron traps, resulting in an increased capacity to store electrons. The release of these electrons occurs gradually following the cessation of excitation, resulting in an increase in the intensity of the afterglow. However, beyond a certain concentration, the high density of electron traps will result in a concentration quenching, and the brightness of the afterglow will be reduced [53–56].

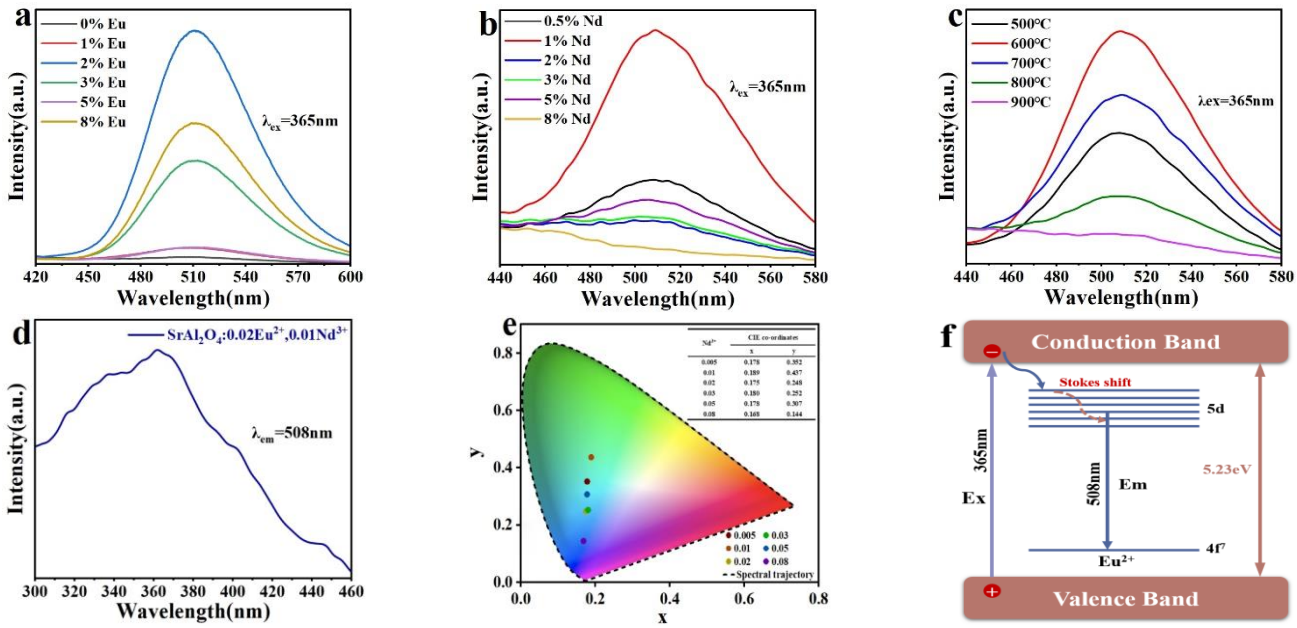

Figure 5. (**a**,**b**) The emission spectra (λ_{ex} = 365 nm) of the $SrAl_2O_4$:xEu^{2+} (x = 0, 0.01, 0.02, 0.03, 0.05, 0.08) and $SrAl_2O_4$:0.02Eu^{2+}, yNd^{3+} (y = 0.005, 0.01, 0.02, 0.03, 0.05, 0.08); (**c**) the emission spectra (λ_{ex} = 365 nm) of the $SrAl_2O_4$:0.02Eu^{2+}, 0.01Nd^{3+} at different sintering temperatures (500–900 °C); (**d**) photoluminescence excitation (PLE) spectra of $SrAl_2O_4$:0.02Eu^{2+}, 0.01Nd^{3+} detected at 508 nm; (**e**) CIE chromaticity plot of the $SrAl_2O_4$:0.02Eu^{2+}, 0.01Nd^{3+} stimulated by 365 nm UV light; (**f**) the luminescent mechanism of Eu^{2+} when stimulated by 365 nm excitation.

The chromaticity diagram can be used to represent the chromatic properties of all colors. According to the spectral trajectory, the color coordinate values corresponding to the spectral tri-stimulus values of the CIE1964 supplemental standard chromaticity observer can be plotted on a CIE1964xy color coordinate chart, as shown in the horseshoe

curve in Figure 5e. The chromaticity diagram can be used to represent the chromaticity characteristics of all colors. The dots on the spectral track represent the spectral colors of different wavelengths, which are the most saturated colors, and the closer to the center of the chromaticity diagram (the white dot), the less saturated the colors. Different angles of rotation around the center of the chromaticity diagram correspond to different wavelengths of the spectral colors, representing different shades. The CIE chromaticity coordinates x and y can be determined using the following equation [57]:

$$x = \frac{X}{X + Y + Z} \tag{2}$$

$$y = \frac{Y}{X + Y + Z} \tag{3}$$

where X, Y, and Z are the CIE tristimulus values. The CIE1964xy color coordinate values were obtained by calculating the spectral data of the samples with different Nd^{3+} ion doping concentrations, as shown in Figure 5e. It can be seen that the color is green at an Nd^{3+} ion concentration of 0.01 and the coordinates are (x = 0.189, y = 0.437); as the concentration increases, the color shifts to blue, and when the doping concentration is 0.08, the coordinates are (x = 0.168, y = 0.144).

Figure 5f illustrates the luminescent mechanism of Eu^{2+} when stimulated by 365 nm excitation. Upon exposure to UV lamp irradiation, the material absorbs photon energy, leading to the excitation of electrons and subsequent 4f-5d transitions. Upon cessation of excitation, the ion undergoes a transition from the 5d excited state to the ground state of the 4f orbital, resulting in the emission of energy and the generation of light. The emission wavelength is determined by the energy level configuration of the ion and its chemical surroundings in the material. When rare earth ions transition from the excited state to the ground state, they release photons. The emitted light often has a longer wavelength than the absorbed light, a phenomenon known as the Stokes shift.

3.5. UV–Vis Diffuse Reflectance

The UV diffuse reflectance spectra of $SrAl_2O_4$:0.02Eu^{2+} and $SrAl_2O_4$:0.02Eu^{2+}, 0.01Nd^{3+} phosphors, which were prepared at 600 °C, are depicted in Figures 6a and 6b, respectively, within the 200–800 nm range. The absorption characteristics and bandgap values of $SrAl_2O_4$:Eu^{2+}, Nd^{3+} were determined through analyzing and calculating its absorption spectrum. The wide absorption band generated by the material at 300–400 nm corresponds to the 4f→5d transition of Eu^{2+}, as shown in the figure. The luminescence performance of the material is strongly correlated with its bandgap value, and it has been established through a review of the existing literature that $SrAl_2O_4$ possesses a direct bandgap. A spectrum was generated using the Tauc formula to determine the bandgap value of the material, based on the measurement data of the material's UV diffuse reflectance spectrum. The Tauc formula can be expressed as [58,59]:

$$(\alpha h\nu)^2 = A\left(h\nu - E_g\right) \tag{4}$$

where A is constant, $h\nu$ is the photon energy, α is the optical absorption coefficient. The insets in Figure 6a,b show the Tauc curves for the two materials, reflecting the $(\alpha h\nu)^2$ versus the energy. The bandgap of synthesized $SrAl_2O_4$:0.02Eu^{2+} and $SrAl_2O_4$:0.02Eu^{2+}, 0.01Nd^{3+} was calculated to be 5.23 eV and 4.98 eV, respectively.

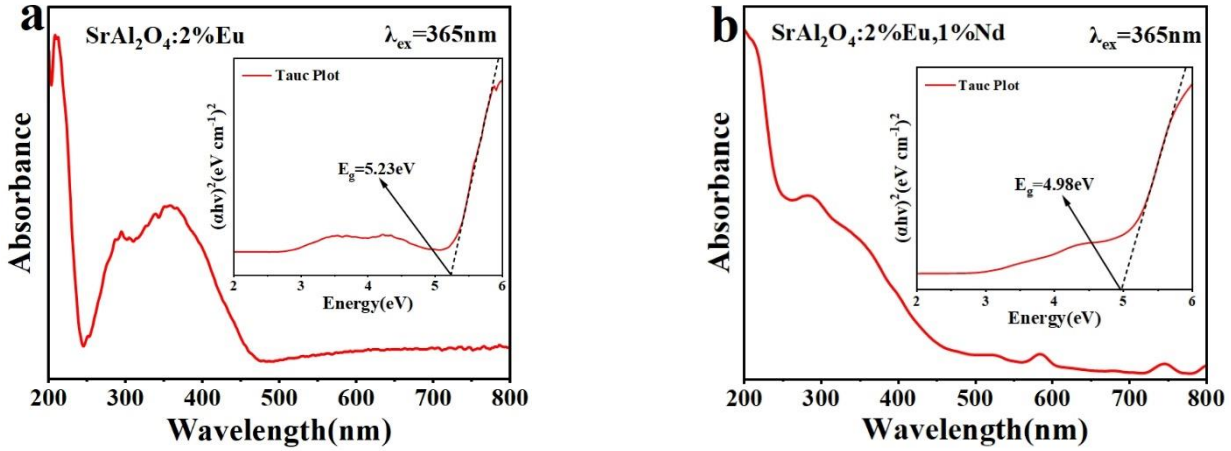

Figure 6. UV absorption spectrum and the bandgap of (**a**) $SrAl_2O_4$:0.02Eu^{2+}; (**b**) $SrAl_2O_4$:0.02Eu^{2+}, 0.01Nd^{3+}.

3.6. Photoluminescence Quantum Yield (PLQY)

Photoluminescence quantum yield (*PLQY*) is the ratio of the number of photons emitting secondary radiated fluorescence to the number of photons absorbing primary radiated photons of excitation light per unit time. This concept is used to quantify the ability of a substance to emit fluorescence after absorbing light energy and is an essential parameter for luminescent materials. The following equation can be used to calculate the quantum yield by combining the measured number of emitted photons (ε) and the number of absorbed photons (α) of the sample [60]:

$$PLQY = \varepsilon/\alpha = \frac{S_{em}}{S_0 - S} \quad (5)$$

where S_{em} represents the total intensity of the emitted light from the phosphor, and S_0 and S represent the total intensity of the scattered light from the reference background plate and the phosphor, respectively. Figure 7 shows a schematic diagram of the quantum yield of three phosphors, $SrAl_2O_4$, $SrAl_2O_4$:0.02Eu^{2+}, and $SrAl_2O_4$:0.02Eu^{2+}, 0.01Nd^{3+}, under the excitation light of 365 nm, with the red color representing the samples and the black color representing the reference white board, and the difference in the area between the scatter range (355 nm–375 nm) and the emission range (400 nm–800 nm) is the quantum yield.

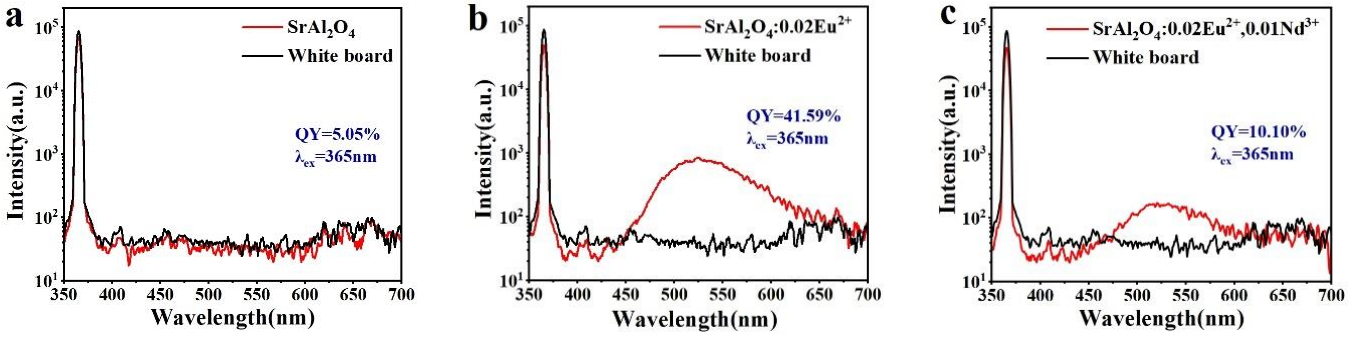

Figure 7. The quantum yield curves of (**a**) $SrAl_2O_4$; (**b**) $SrAl_2O_4$:0.02Eu^{2+}; and (**c**) $SrAl_2O_4$:0.02Eu^{2+}, 0.01Nd^{3+}.

The plots show quantum yields of 5.05%, 41.59%, and 10.10% for $SrAl_2O_4$, $SrAl_2O_4$:0.02Eu^{2+}, and $SrAl_2O_4$:0.02Eu^{2+}, 0.01Nd^{3+}, respectively. It is evident that the doping of rare earth ions greatly enhances the quantum yield of the material and improves its luminescence ability, indicating that the special structure of Eu^{2+} ions can effectively realize the transfer of energy, which can substantially improve the quantum yield [61,62]. The

quantum yield of the $SrAl_2O_4$:0.02Eu^{2+} sample is slightly lower [63], and we will focus on this aspect in our future work. The low quantum yields of the sample doped with Nd^{3+} ions can be attributed to the introduction of non-radiative dissipation channels by the addition of Nd^{3+} ions. These ions have the ability to absorb a portion of the energy into their energy levels, resulting in a loss in quantum yield [64,65].

3.7. Fluorescence Lifetime and Afterglow Decay

The fluorescence lifetime is the duration of time required for the fluorescence intensity of a material to decrease to 1/e of its initial value after the excitation light source is removed. Figure 8 shows the fluorescence decay curves and the fitted curves of $SrAl_2O_4$:0.02Eu^{2+}, yNd^{3+} (y = 0.005, 0.01, 0.02, 0.03, 0.05) at 365 nm excitation wavelength, including the initial rapid decay and the subsequent slow decay. A third-order exponential function can be used to estimate the fluorescence decay curve [66]:

$$I(t) = I_0 + A_1 e^{-\frac{t}{\tau 1}} + I_0 + A_2 e^{-\frac{t}{\tau 2}} + A_3 e^{-\frac{t}{\tau 3}} \quad (6)$$

where I is the phosphorescence intensity; I_0, A_1, A_2, and A_3 are constants; t is the time; τ_1, τ_2, and τ_3 are the exponential component decay times. The above values can be calculated by Origin software, as shown in Table 3. The average decay time τ* of $SrAl_2O_4$ under different Nd^{3+} doping concentrations can be obtained using the following equation [67]:

$$\tau_{ave} = \frac{A_1 {\tau_1}^2 + A_2 {\tau_2}^2 + A_3 {\tau_3}^2}{A_1 \tau_1 + A_2 \tau_2 + A_3 \tau_3} \quad (7)$$

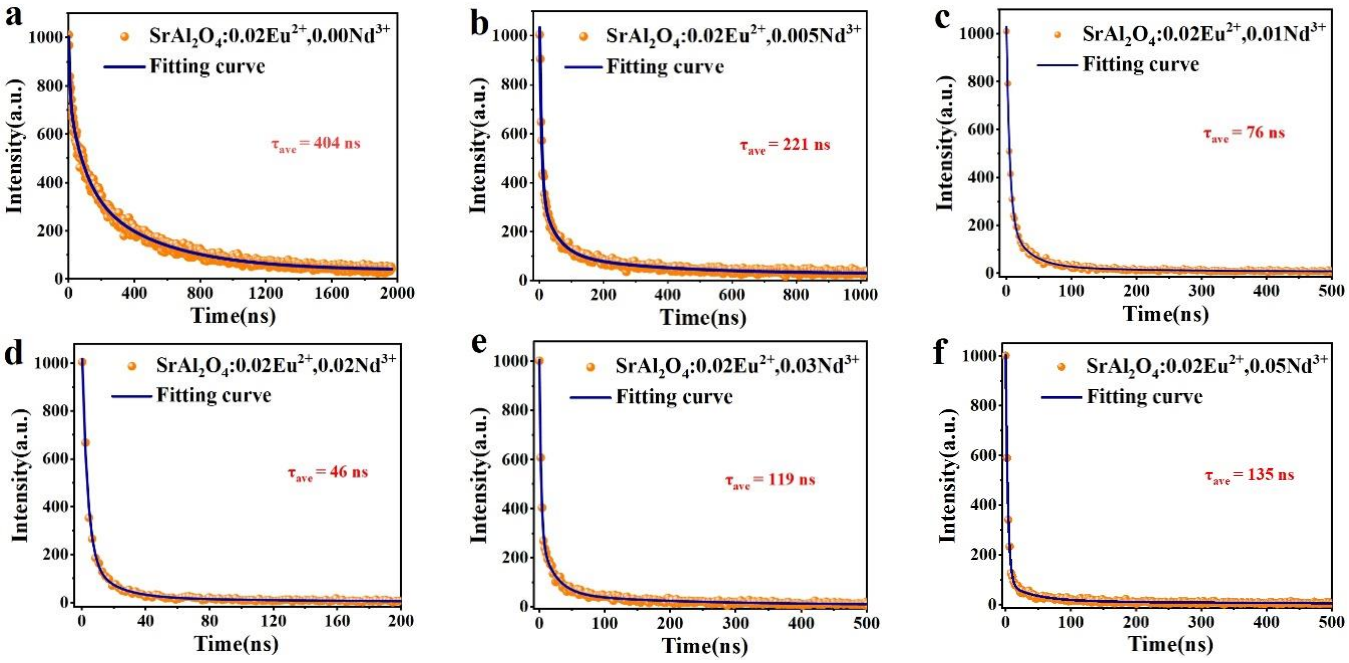

Figure 8. (**a**–**f**) The fluorescence lifetime decay curves and fitting curves of $SrAl_2O_4$:0.02Eu^{2+}, xNd^{3+} (x = 0, 0.005, 0.01, 0.02, 0.03, 0.05) phosphors.

The average decay times τ* of $Sr_{0.98-y}Al_2O_4$:0.02Eu^{2+}, yNd^{3+} (y = 0, 0.005, 0.01, 0.02, 0.03, 0.05) were calculated from the above equation as 404 ns, 221 ns, 76 ns, 46 ns, 119 ns, and 135 ns, respectively. The fluorescence lifetime of the $SrAl_2O_4$:0.02Eu^{2+} sample is similar to that of the sample prepared by the high-temperature solid-phase method [68]. From Figure 8, the longest fluorescence lifetime is observed in the $SrAl_2O_4$:0.02Eu^{2+} phosphor, which begins to decrease as the concentration of Nd^{3+} doping increases; this is due to the formation of trap centers when Nd^{3+} replaces Sr^{2+} in the matrix, capturing some electrons. The phosphor's fluorescence lifetime begins to decay as the concentration of Nd^{3+} ions

continues to rise, which may be related to the high density of electron traps, which produces the concentration quenching phenomenon.

Table 3. The average fluorescence lifetime of $SrAl_2O_4$:0.02Eu^{2+}, xNd^{3+} (x = 0, 0.005, 0.01, 0.02, 0.03, 0.05) phosphors.

Nd^{3+}	Decay Lifetimes (ns)						
	A_1	τ_1	A_2	τ_2	A_3	τ_3	τ^*
0.00	256	8	343	96	367	468	404
0.005	668	6	250	48	88	325	221
0.01	804	5	195	30	24	193	76
0.02	169	17	825	3	22	121	46
0.03	719	3	231	22	48	196	119
0.05	69	41	919	3	13	301	135

To conduct a more detailed examination of the afterglow properties of the phosphors, we analyzed the decay curves of the afterglow for $SrAl_2O_4$:0.02Eu^{2+}, 0.01Nd^{3+}, and $SrAl_2O_4$:0.02Eu^{2+}, 0.02Nd^{3+} at an excitation wavelength of 365 nm. The fluorescence decay curves and the calculation of the average afterglow duration are based on Equations (5) and (6) for the third-order exponential fitting, and the parameters are shown in Table 4. Similarly, the decay processes of the samples are categorized into two types: early rapid decay and subsequent gradual decay. The rapid decay process dominates the intensity and the slow decay process is also known as the long afterglow luminescence process [69]. As depicted in Figure 9, the average afterglow duration τ^* of $SrAl_2O_4$:0.02Eu^{2+}, 0.01Nd^{3+} is 13 s, while the average afterglow duration of $SrAl_2O_4$:0.02Eu^{2+}, 0.02Nd^{3+} is 8 s. The reason why the afterglow is produced for a shorter period of time is because the energy is dissipated too quickly during the energy transfer process. This phosphor can rapidly transfer energy to the surrounding area through non-radiant energy transfer, which greatly improves the efficiency. Based on this property, these phosphors are well suited for fluorescent signal detection as well as anti-counterfeiting applications [70,71].

Table 4. Afterglow decay time for $SrAl_2O_4$:0.02Eu^{2+}, 0.01Nd^{3+} and $SrAl_2O_4$:0.02Eu^{2+}, 0.02Nd^{3+} samples.

Nd^{3+}	Afterglow Decay Time (s)						
	A_1	τ_1	A_2	τ_2	A_3	τ_3	τ^*
0.01	33,392	2	53,015	0	6063	15	8
0.02	709	1	1503	0	85	21	13

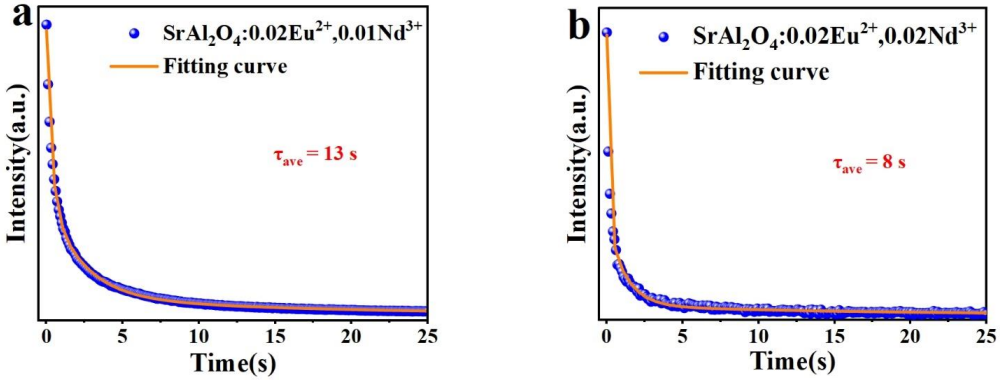

Figure 9. The afterglow decay curves and fitting curves of (**a**) $SrAl_2O_4$:0.02Eu^{2+}, 0.01Nd^{3+} and (**b**) $SrAl_2O_4$:0.02Eu^{2+}, 0.02Nd^{3+} phosphors after exposure to a 365 nm UV light for 3 min.

3.8. Anti-Counterfeiting Application

In order to confirm the potential application of the prepared phosphors in anti-counterfeiting printing, we combined the $SrAl_2O_4$:0.02Eu^{2+} and $SrAl_2O_4$:0.02Eu^{2+}, 0.01Nd^{3+} fluorescent powders separately with polyacrylic acid and ethanol to create two types of anti-counterfeiting ink. The butterfly and ladybug patterns were printed through screen printing. As depicted in Figure 10, it can be observed that the pattern does not show color under fluorescent light, and the printed pattern can be clearly seen under the irradiation of a 365 nm UV lamp. The color of $SrAl_2O_4$:0.02Eu^{2+} fluorescent ink disappears after turning off the UV lamp, but the $SrAl_2O_4$:0.02Eu^{2+}, 0.01Nd^{3+} fluorescent ink can continue to emit light for a period of time. Therefore, we can consider the prepared luminescent material as having a significant potential for application in the domain of anti-counterfeit printing.

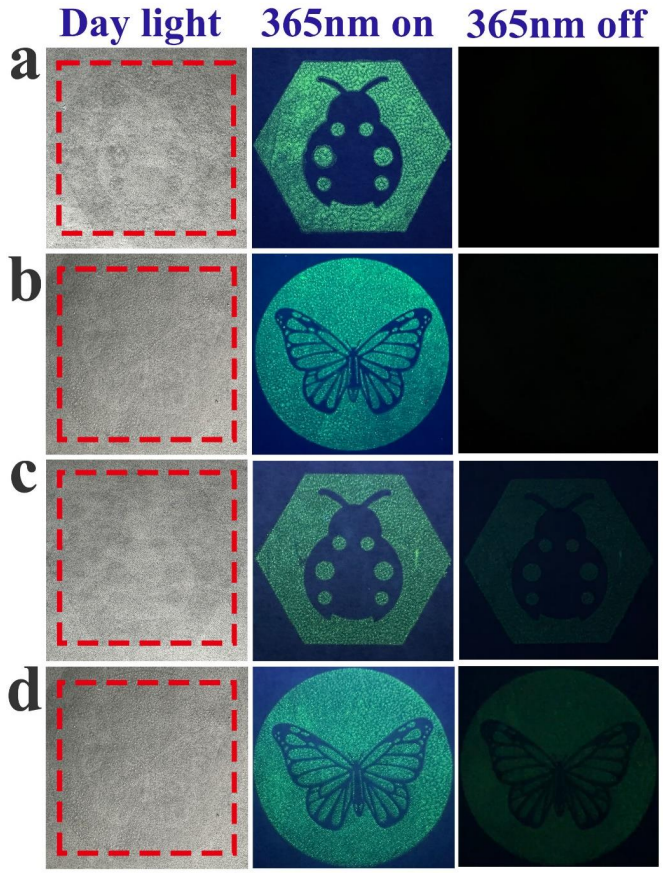

Figure 10. The (**a**) ladybug and (**b**) butterfly patterns printed with $SrAl_2O_4$:0.02Eu^{2+} ink; the (**c**) ladybug and (**d**) butterfly patterns printed with $SrAl_2O_4$:0.02Eu^{2+}, 0.01Nd^{3+} ink.

4. Conclusions

In conclusion, the combustion method was employed to produce a series of $SrAl_2O_4$:0.02Eu^{2+} and $SrAl_2O_4$:0.02Eu^{2+}, 0.01Nd^{3+} phosphors. The successful doping of Eu^{2+} and Nd^{3+} ions into the $SrAl_2O_4$ host was demonstrated by XRD, EDS, and XPS characterization tests. Photoluminescence tests were carried out on the phosphors, and the results showed that both $SrAl_2O_4$:Eu^{2+} and $SrAl_2O_4$:Eu^{2+}, Nd^{3+} exhibited green luminescence when exposed to 365 nm excitation light, with a peak emission at 508 nm, which is caused by the $4f^65d^1 \rightarrow 4f^7$ transition of Eu^{2+}. The fluorescence lifetimes of $SrAl_2O_4$:0.02Eu^{2+} and $SrAl_2O_4$:0.02Eu^{2+}, 0.01Nd^{3+} were 404 ns and 76 ns and the quantum yields were 41.59% and 10.10%. The Nd^{3+}-doped samples showed strong afterglow performance with an afterglow lifetime of 13s. The bandgap values of the samples were measured by plotting Tauc curves from UV diffuse reflectance spectra, which matched the calculated bandgap values. $SrAl_2O_4$:0.02Eu^{2+} and $SrAl_2O_4$:0.02Eu^{2+}, 0.01Nd^{3+} phosphors were prepared for

anti-counterfeiting inks, and better anti-counterfeiting effects were obtained by printing the patterns by screen printing.

Author Contributions: Methodology, Z.W., Q.L. and J.L.; Software, Z.W., J.W., J.L., C.L. and R.W.; Validation, C.L.; Formal analysis, Z.W. and Y.Q.; Investigation, Z.Z. and R.W.; Resources, Y.Q.; Data curation, Z.L. and Z.Z.; Writing—original draft, Z.W.; Writing—review & editing, Z.W., Q.L., J.W. and X.W.; Funding acquisition, Q.L., J.W. and Z.L. All authors have read and agreed to the published version of the manuscript.

Funding: This research is supported by the National Key R&D Program of China (grant No. 2021YFC2802000), the National key research and development program (2019YFB1707202), Beijing Natural Science Foundation (No. 2202018), the General Project of Beijing Municipal Education Commission Science and Technology Program (No. KM202010015004), the National Natural Science Foundation of China (Nos. 21604005 and 52072084), the general project of fundamental research of BIGC (No. Ed202208).

Data Availability Statement: Data is contained within the article.

Conflicts of Interest: Authors Zhanwei Zhang, Xinfeng Wang, Cuijuan Li, Rong Wang were employed by Yunnan Jiake Packaging Technology Co., Ltd. The remaining authors declare that the research was conducted in the absence of any commercial or financial relationships that could be construed as a potential conflict of interest.

References

1. Vaidyanathan, S. Recent progress on lanthanide-based long persistent phosphors: An overview. *J. Mater. Chem. C* **2023**, *11*, 8649–8687. [CrossRef]
2. Shen, S.; Xie, Q.; Sahoo, S.R.; Jin, J.; Baryshnikov, G.V.; Sun, H.; Wu, H.; Ågren, H.; Liu, Q.; Zhu, L. Edible Long-Afterglow Photoluminescent Materials for Bioimaging. *Adv. Mater.* **2024**, *36*, 2404888. [CrossRef] [PubMed]
3. Hai, O.; Pei, M.; Yang, E.; Ren, Q.; Wu, X.; Zhu, J.; Zhao, Y.; Du, L. Exploration of long afterglow luminescence materials work as round-the-clock photocatalysts. *J. Alloys Compd.* **2021**, *866*, 158752. [CrossRef]
4. Guo, Y.; Wang, Q.; Liu, S.; Ya, W.; Qi, P.; Ni, Z.; Liu, H.; Zhang, Q. A brief review: The application of long afterglow luminescent materials in environmental remediation. *RSC Adv.* **2023**, *13*, 16145–16153. [CrossRef] [PubMed]
5. Kuang, Q.; Hou, X.; Du, C.; Wang, X.; Gao, D. Recent advances in the anti-counterfeiting applications of long persistent phosphors. *Phys. Chem. Chem. Phys.* **2023**, *25*, 17759–17768. [CrossRef] [PubMed]
6. Wu, Y.; Li, P.; Guan, M.; Guo, Y.; Xu, S.; Zhang, J. Observation of tunable persistent luminescence in XAl_2O_4: Eu^{2+} (X = Ca, Sr) doped borate glass for efficient optical information storage. *Ceram. Int.* **2023**, *49*, 30461–30470. [CrossRef]
7. Zhai, B.-G.; Huang, Y.-M. Green Afterglow of Undoped $SrAl_2O_4$. *Nanomaterials* **2021**, *11*, 2331. [CrossRef] [PubMed]
8. Matsuzawa, T.; Aoki, Y.; Takeuchi, N.; Murayama, Y. A New Long Phosphorescent Phosphor with High Brightness, $SrAl_2O_4$:Eu^{2+},Dy^{3+}. *J. Electrochem. Soc.* **2019**, *143*, 2670–2673. [CrossRef]
9. Gao, P.; Wang, J.; Wu, J.; Xu, Q.; Yang, L.; Liu, Q.; Qi, Y.; Li, Z. Preparation of $SrAl_2O_4$: Eu^{2+}, Dy^{3+} Powder by Combustion Method and Application in Anticounterfeiting. *Coatings* **2023**, *13*, 808. [CrossRef]
10. Lazău, R.; Ianoș, R.; Păcurariu, C.; Căpraru, A. Comparative study on $SrAl_2O_4$ formation using different approaches. *Ceram. Int.* **2022**, *48*, 13271–13276. [CrossRef]
11. Zhai, B.-g.; Huang, Y.M. Green photoluminescence and afterglow of Tb-doped $SrAl_2O_4$. *J. Mater. Sci.* **2016**, *52*, 1813–1822. [CrossRef]
12. Sasikumar, P.; Gopalan, A.; Pugazhendhi, S.; Vimalan, M.; Abbas, M. Tunable luminescence and electrical properties of cerium doped strontium aluminate ($SrAl_2O_4$: Ce^{3+}) phosphors for white LED applications. *Heliyon* **2023**, *9*, E17429.
13. Sera, M.; Yamamoto, M.; Tomita, K.; Yabara, Y.; Izawa, S.; Hiramoto, M.; Nakanishi, T.; Yoshida, K.; Nishiyama, K. Morphology control and synthesis of afterglow materials with a $SrAl_2O_4$ framework synthesized by Surfactant-Template and hydrothermal methods. *Chem. Phys. Lett.* **2021**, *780*, 138916. [CrossRef]
14. Thomas, N.M.; Anila, E.I. Synthesis and Characterisation of $SrAl_2O_4$: Eu^{3+} Orange-Red Emitting Nanoparticles. *J. Fluoresc.* **2023**, *34*, 1161–1169. [CrossRef] [PubMed]
15. Ge, W.; Gao, W.; Tian, Y.; Zhang, P.; Zhu, J.; Li, Y. Tunable dual-mode photoluminescences from $SrAl_2O_4$: Eu/Yb nanofibers by different atmospheric annealing. *J. Alloys Compd.* **2021**, *859*, 158261. [CrossRef]
16. Kaur, P.; Khanna, A. Structural, thermal and light emission properties of Eu, Sm, Dy, Er and Mn doped $CaAl_2O_4$ and $SrAl_2O_4$. *Ceram. Int.* **2021**, *47*, 14655–14664. [CrossRef]
17. Singh, S.; Tanwar, V.; Simantilleke, A.P.; Singh, D. Structural and photoluminescent investigations of $SrAl_2O_4$:Eu^{2+}, RE^{3+} improved nanophosphors for solar cells. *Nano-Struct. Nano-Objects* **2020**, *21*, 100427.
18. Li, Z.; Hao, S.; Ji, W.; Hao, L.; Yin, L.; Xu, X.; Agathopoulos, S. Mechanism of long afterglow in $SrAl_2O_4$: Eu phosphors. *Ceram. Int.* **2021**, *47*, 32947–32953. [CrossRef]

19. Ryu, H.; Bartwal, K.S. Defect structure and its relevance to photoluminescence in $SrAl_2O_4$:Eu^{2+}, Nd^{3+}. *Phys. B Condens. Matter* **2009**, *404*, 1714–1718. [CrossRef]
20. Marchal, M.; Escribano, P.; Carda, J.B.; Cordoncillo, E.; Vallet-Regí, M.; Conde, F.; Sánchez, J.; de Andrés, A. Long-Lasting Phosphorescent Pigments of the Type $SrAl_2O_4$ Eu^{2+}, R^{3+} (R = Dy, Nd) Synthesized by the Sol-Gel Method. *J. Sol-Gel Sci. Technol.* **2003**, *26*, 989–992. [CrossRef]
21. Rakesh, N. Essentials of pharmaceutical packaging to prevent drug counterfeiting. *Int. J. Sci. Res. Arch.* **2023**, *9*, 599–605. [CrossRef]
22. Nguyen, H.P.; Retraint, F.; Morain-Nicolier, F.; Delahaies, A. A Watermarking Technique to Secure Printed Matrix Barcode—Application for Anti-Counterfeit Packaging. *IEEE Access* **2019**, *7*, 131839–131850. [CrossRef]
23. Wang, Z.; Jiang, L.; Li, X.; Li, B.; Zhou, S.; Xu, Z.; Huang, L. Thermally Reconfigurable Hologram Fabricated by Spatially Modulated Femtosecond Pulses on a Heat-Shrinkable Shape Memory Polymer for Holographic Multiplexing. *ACS Appl. Mater. Interfaces* **2021**, *13*, 51736–51745. [CrossRef] [PubMed]
24. Li, P.; Yang, J.; Jiménez-Carvelo, A.M.; Erasmus, S.W. Applications of food packaging quick response codes in information transmission toward food supply chain integrity. *Trends Food Sci. Technol.* **2024**, *146*, 104384. [CrossRef]
25. Muthamma, K.; Sunil, D. Cellulose as an Eco-Friendly and Sustainable Material for Optical Anticounterfeiting Applications: An Up-to-Date Appraisal. *ACS Omega* **2022**, *7*, 42681–42699. [CrossRef] [PubMed]
26. Mardani, H.; Bayrak, E.; Özçelik, Ş.; Babazadeh-Mamaqani, M.; Kahveci, M.U.; Roghani-Mamaqani, H.; Salami-Kalajahi, M. Anti-counterfeiting ink based on polymer nanoparticles containing spiropyran and Aza-BODIPY for artificial industries. *React. Funct. Polym.* **2023**, *187*, 105593. [CrossRef]
27. Zhou, S.; Wang, Y.; Hu, P.; Zhong, W.; Jia, H.; Qiu, J.; Fu, J. Cascaded Photon Confinement-Mediated Orthogonal RGB-Switchable $NaErF_4$-Cored Upconversion Nanoarchitectures for Logicalized Information Encryption and Multimodal Luminescent Anti-Counterfeiting. *Laser Photonics Rev.* **2022**, *17*, 2200531. [CrossRef]
28. Jiang, Z.; Cheng, H.; Lai, F.; Xiao, Z.; Chen, J.; Sun, J.; You, W. Preparation, luminescence properties, and application of temperature sensing and anti-counterfeiting of La_2MgTiO_6: Yb^{3+}/Ln^{3+}/Mn^{4+}. *J. Am. Ceram. Soc.* **2022**, *105*, 4731–4743. [CrossRef]
29. Zhang, C.; Yin, Q.; Ge, S.; Qi, J.; Han, Q.; Gao, W.; Wang, Y.; Zhang, M.; Dong, J. Optical anti-counterfeiting and information storage based on rare-earth-doped luminescent materials. *Mater. Res. Bull.* **2024**, *176*, 112801. [CrossRef]
30. Chen, Q.; Jiang, J.; Zhang, H.; Fu, H.; Liu, W.; Zheng, J. Yb^{3+}/Eu^{3+}/Ho^{3+} Tridoped $Cs_2Ag_{0.3}Na_{0.7}InC_{l6}$ Double Perovskite with Excitation-Wavelength-Dependent Triple Emission for Anti-Counterfeiting Application. *Crystals* **2022**, *13*, 13.
31. Liu, Z.; Yang, X.; Yu, X.; Xiao, J.; Zhang, P.; Liu, D.; Zhang, J.; Xu, X.; Qiu, J. Design opto-thermo-mechano-multi-responsive luminescence from $Sr_4Al_{14}O_{25}$: Eu^{2+}, Nd^{3+}, Tm^{3+} for optical information storage. *Ceram. Int.* **2024**, *50*, 9840–9847. [CrossRef]
32. Meng, S.; Li, A.; Li, K.; Song, Y.; Qin, Z.; Zhang, R.; Zhang, Y.; Ren, W.; Yang, W. First-Principles Investigations of the Electronic Structure and Mechanical Characteristics of Nd^{3+}-Doped $YAlO_3$ Crystals. *Crystals* **2024**, *14*, 293. [CrossRef]
33. Jang, M.-K.; Cho, Y.-S.; Huh, Y.-D. Photoluminescence properties of Eu^{2+} activator ions in the SrS–Ga_2S_3 system. *J. Alloys Compd.* **2020**, *828*, 154424. [CrossRef]
34. Tian, M.; Wang, Z.; Li, W.; Wang, C.; Cheng, J.; Li, Z.; Yang, Z.; Li, P. Regulation defect and Eu2+ luminescence via cation substitution in Ca_2BO_3Cl: Eu^{2+}, M^{2+} (M = Sr and Ba) for white LEDs. *J. Alloys Compd.* **2019**, *787*, 1004–1014. [CrossRef]
35. Aly, K.A.; Khalil, N.M.; Algamal, Y.; Saleem, Q.M.A. Lattice strain estimation for $CoAl_2O_4$ nano particles using Williamson-Hall analysis. *J. Alloys Compd.* **2016**, *676*, 606–612. [CrossRef]
36. Romero, M.; Rosas-Huerta, J.L.; Benitez-Rico, A.; Minaud, C.; Arévalo-López, E.P.; Escamilla, R. Molten salts synthesis of double perovskite $Sr_{2-x}Gd_xFeNbO_6$: Structure, magnetic properties and XPS study. *Phys. B Condens. Matter* **2023**, *655*, 414752. [CrossRef]
37. Komai, S.; Hirano, M.; Ohtsu, N. Spectral analysis of Sr 3d XPS spectrum in Sr-containing hydroxyapatite. *Surf. Interface Anal.* **2020**, *52*, 823–828. [CrossRef]
38. Gültekin, S.; Yıldırım, S.; Yılmaz, O.; Keskin, İ.Ç.; Katı, M.İ.; Çelik, E. Structural and optical properties of $SrAl_2O_4$: Eu^{2+}/Dy^{3+} phosphors synthesized by flame spray pyrolysis technique. *J. Lumin.* **2019**, *206*, 59–69. [CrossRef]
39. Cortés-Adasme, E.; Castillo, R.; Conejeros, S.; Vega, M.; Llanos, J. Behavior of Eu ions in $SrSnO_3$: Optical properties, XPS experiments and DFT calculations. *J. Alloys Compd.* **2019**, *771*, 162–168. [CrossRef]
40. Crist, B.V. XPS in industry—Problems with binding energies in journals and binding energy databases. *J. Electron Spectrosc. Relat. Phenom.* **2019**, *231*, 75–87. [CrossRef]
41. Moseenkov, S.I.; Kuznetsov, V.L.; Zolotarev, N.A.; Kolesov, B.A.; Prosvirin, I.P.; Ishchenko, A.V.; Zavorin, A.V. Investigation of Amorphous Carbon in Nanostructured Carbon Materials (A Comparative Study by TEM, XPS, Raman Spectroscopy and XRD). *Materials* **2023**, *16*, 1112. [CrossRef]
42. Hamdi, D.; Talantikite-Touati, D.; Manseri, A.; Khodja, A.T.; Souici, A. Role of Nd doping on the structural, morphological and optical properties of $BaTiO_3$ nanoparticles hydrothermally synthesized. *Opt. Mater.* **2024**, *152*, 115387. [CrossRef]
43. Dudric, R.; Bortnic, R.; Souca, G.; Ciceo-Lucacel, R.; Stiufiuc, R.; Tetean, R. XPS on $Nd_{0.6}$-Bi $Sr_{0.4}MnO_3$ nano powders. *Appl. Surf. Sci.* **2019**, *487*, 17–21. [CrossRef]
44. Sharma, V.; Das, A.; Kumar, V. Eu^{2+}, Dy^{3+} codoped $SrAl_2O_4$nanocrystalline phosphor for latent fingerprint detection in forensic applications. *Mater. Res. Express* **2016**, *3*, 015004. [CrossRef]
45. Das, S.; Manam, J.; Sharma, S.K. Composites of $BaAl_2O_4$: Eu^{2+},Dy^{3+}/organic dye encapsulated in mesoporous silica as multicolor long persistent phosphors based on radiative energy transfer. *New J. Chem.* **2017**, *41*, 5934–5941. [CrossRef]

46. Gedekar, K.A.; Wankhede, S.P.; Moharil, S.V.; Belekar, R.M. d–f luminescence of Ce^{3+} and Eu^{2+} ions in $BaAl_2O_4$, $SrAl_2O_4$ and $CaAl_2O_4$ phosphors. *J. Adv. Ceram.* **2017**, *6*, 341–350. [CrossRef]
47. Li, X.; Zhu, X.; Li, J.; Liu, P.; Huang, M.; Xiang, B. Phytic acid-derived Co_2P/N-doped carbon nanofibers as flexible free-standing anode for high performance lithium/sodium ion batteries. *J. Alloys Compd.* **2020**, *846*, 156256. [CrossRef]
48. Chen, H.; Ju, L.; Zhang, L.; Wang, X.; Zhang, L.; Xu, X.; Gao, L.; Qiu, K.; Yin, L. Exploring a particle-size-reduction strategy of YAG: Ce phosphor via a chemical breakdown method. *J. Rare Earths* **2021**, *39*, 938–945. [CrossRef]
49. Ryou, Y.; Lee, J.; Lee, H.; Kim, C.H.; Kim, D.H. Effect of various activation conditions on the low temperature NO adsorption performance of Pd/SSZ-$_{13}$ passive NOx adsorber. *Catal. Today* **2019**, *320*, 175–180. [CrossRef]
50. Ning, L.; Huang, X.; Huang, Y.; Tanner, P.A. Origin of the green persistent luminescence of Eu-doped $SrAl_2O_4$from a multiconfigurationalab initiostudy of 4f7→4f65d1transitions. *J. Mater. Chem. C* **2018**, *6*, 6637–6640. [CrossRef]
51. Parauha, Y.R.; Dhoble, S.J. Photoluminescence and electron-vibrational interaction in 5d state of Eu^{2+} ion in $Ca_3Al_2O_6$ down-conversion phosphor. *Opt. Laser Technol.* **2021**, *142*, 107191. [CrossRef]
52. Jamshidijam, M.; Thangaraj, P.; Akbari-Fakhrabadi, A.; Niño Galeano, M.A.; Usuba, J.; Viswanathan, M.R. Influence of rare earth (RE = Nd, Y, Pr and Er) doping on the microstructural and optical properties of ceria nanostructures. *Ceram. Int.* **2017**, *43*, 5216–5222. [CrossRef]
53. Zhang, X.; Su, J.; Yan, X.; Liao, Y.; Wu, Z.-c.; Zhou, C. Concentration quenching and thermal stability of Eu^{2+} emission in green emitting phosphor Li_2BaSiO_4: Eu^{2+}. *Solid State Sci.* **2020**, *99*, 106050. [CrossRef]
54. Wang, Z.; Meijerink, A. Concentration Quenching in Upconversion Nanocrystals. *J. Phys. Chem. C Nanomater. Interfaces* **2018**, *122*, 26298–26306. [CrossRef] [PubMed]
55. Khan, S.; Mohapatra, S.K.; Chakraborty, S.; Annapurna, K. Energy transfer mechanisms and non-radiative losses in Nd^{3+} doped phosphate laser glass: Dopant concentration effect study. *Opt. Mater.* **2023**, *143*, 114229. [CrossRef]
56. Soto, X.L.; Swierk, J.R. Using Lifetime and Quenching Rate Constant to Determine Optimal Quencher Concentration. *ACS Omega* **2022**, *7*, 25532–25536. [CrossRef] [PubMed]
57. Lee, W.; Kim, S.; Lee, S.; Kim, S. Technical note: Usability evaluation of the modified CIE1976 Uniform-Chromaticity scale for assessing image quality of visual display monitors. *Hum. Factors Ergon. Manuf. Serv. Ind.* **2003**, *13*, 85–95. [CrossRef]
58. Tauc, J. Optical properties and electronic structure of amorphous Ge and Si. *Mater. Res. Bull.* **1968**, *3*, 37–46. [CrossRef]
59. Liu, B.; Gu, M.; Liu, X.; Huang, S.; Ni, C. Theoretical study of structural, electronic, lattice dynamical and dielectric properties of $SrAl_2O_4$. *J. Alloys Compd.* **2011**, *509*, 4300–4303. [CrossRef]
60. Zhang, Y.; Qiao, X.; Wan, J.; Wu, L.-a.; Chen, B.; Fan, X. Facile synthesis of monodisperse YAG:Ce^{3+} microspheres with high quantum yield via an epoxide-driven sol–gel route. *J. Mater. Chem. C* **2017**, *5*, 8952–8957. [CrossRef]
61. Yang, S.; Dai, Y.; Shen, Y.; Duan, C.; Rao, Q.; Peng, H.; Yang, F.; Shan, Y.; Zhao, Q. Blue emission from $Sr_{0.98}Ga_2B_2O_7$: 0.01Bi^{3+}, 0.01Dy^{3+} phosphor with high quantum yield. *J. Alloys Compd.* **2019**, *810*, 151849.
62. Kim, D.; Seo, Y.W.; Park, S.H.; Choi, B.C.; Kim, J.H.; Jeong, J.H. Theoretical design and characterization of high efficient $Sr_9Ln(PO_4)_7$: Eu^{2+} phosphors. *Mater. Res. Bull.* **2020**, *127*, 110856. [CrossRef]
63. Gao, P.; Liu, Q.; Wu, J.; Jing, J.; Zhang, W.; Zhang, J.; Jiang, T.; Wang, J.; Qi, Y.; Li, Z. Enhanced Fluorescence Characteristics of $SrAl_2O_4$: Eu^{2+}, Dy^{3+} Phosphor by Co-Doping Gd^{3+} and Anti-Counterfeiting Application. *Nanomaterials* **2023**, *13*, 2034. [CrossRef]
64. Möller, S.; Hoffmann, A.; Knaut, D.; Flottmann, J.; Jüstel, T. Determination of vis and NIR quantum yields of Nd^{3+}-activated garnets sensitized by Ce^{3+}. *J. Lumin.* **2015**, *158*, 365–370. [CrossRef]
65. Dibaba, S.T.; Xiaoqian, G.; Ren, W.; Sun, L. Recent progress of energy transfer and luminescence intensity boosting mechanism in Nd^{3+}-sensitized upconversion nanoparticles. *J. Rare Earths* **2019**, *37*, 791–805. [CrossRef]
66. Yang, L.; Liu, Q.; Zheng, H.; Zhou, S.; Zhang, W. The decay model of Eu^{2+} and Eu^{2+}, Dy^{3+} substituted $SrAl_2O_4$ prepared by high temperature solid phase method. *J. Phys. Chem. Solids* **2019**, *124*, 151–156. [CrossRef]
67. Xie, Q.; Li, B.; He, X.; Zhang, M.; Chen, Y.; Zeng, Q. Correlation of Structure, Tunable Colors, and Lifetimes of (Sr, Ca, Ba)$Al_{(2)}O_{(4)}$: $Eu^{(2+)}$, $Dy^{(3+)}$ Phosphors. *Materials* **2017**, *10*, 1198. [CrossRef] [PubMed]
68. Nakauchi, D.; Kato, T.; Kawaguchi, N.; Yanagida, T. Comparative studies on scintillation properties of Eu-doped $CaAl_2O_4$, $SrAl_2O_4$, and $BaAl_2O_4$ crystals. *Jpn. J. Appl. Phys.* **2022**, *62*, 010607. [CrossRef]
69. Lei, B.; Zhang, H.; Mai, W.; Yue, S.; Liu, Y.; Man, S.-q. Luminescent properties of orange-emitting long-lasting phosphorescence phosphor Ca_2SnO_4: Sm^{3+}. *Solid State Sci.* **2011**, *13*, 525–528. [CrossRef]
70. Qiao, X.; Han, Y.; Tian, D.; Yang, Z.; Li, J.; Zhao, S. MOF matrix doped with rare earth ions to realize ratiometric fluorescent sensing of 2,4,6-trinitrophenol: Synthesis, characterization and performance. *Sens. Actuators B Chem.* **2019**, *286*, 1–8. [CrossRef]
71. Zhao, J.; Zhang, Y.; Wang, T.; Guan, L.; Dong, G.; Liu, Z.; Fu, N.; Wang, F.; Li, X. Preparation and luminescent modulation of $KGaSiO_4$: Eu^{3+} phosphors using for multiple anti-counterfeiting. *Ceram. Int.* **2023**, *49*, 29505–29511. [CrossRef]